Microstructure and properties of a nanostructured W-31 wt% Cu composite produced by magnetic pulse compaction of bimetallic nanoparticles

Alexander Pervikov [1,2], Andrey Filippov [1], Yuri Mironov [1], Mark Kalashnikov[1], Maksim Krinitcyn[1], Dmitry Eskin[2,3], Marat Lerner [1,2] and Sergei Tarasov [1,2]

[1] Institute of Strength Physics and Materials Science SB RAS, Tomsk, Russian Federation
[2] National Research Tomsk State University, Tomsk, Russian Federation
[3] Brunel University London, Uxbridge, United Kingdom

Abstract Nanostructured W-31wt.%Cu composite was for the first time produced via magnetic pulse compaction from bimetallic particles obtained using electric explosion of intertwisted copper/tungsten wires in argon and then characterized for microstructures, mechanical strength and tribological behavior at high temperatures. Microstructure of the composite is characterized by recrystallized copper grains with mean grain size of 59 ± 3 nm and unreacted spherical tungsten particles. The composite density was in the range 93-99%. Flexural and compression strengths were 560 ± 10 and 1035 ± 150 MPa, respectively. Tribological high temperature tests showed that this composite develops reduced wear starting from the testing at 250°C. Such an adaptation mechanisms is related to generation of copper tungstate $CuWO_4$ on the worn surfaces.

1.Introduction

W-Cu pseudoalloys are immiscible metal composites intended to combine high electric and heat conductivities of copper with low thermal expansion and good thermal stability of tungsten. Such a combination allows applying them in electric engineering, welding and even aerospace engineering. The finer the composite components, the better the performance anticipated and, therefore, attempts were made to obtain W-Cu composites with submicron- and nanosized grains [1,2] using such methods as powder metallurgy sintering of nanoparticles [3], arresting the grain boundaries by segregations [4, 5], spark plasma sintering (SPS) [6,7], and severe plastic deformation by high-pressure torsion (HPT) [8-10]. Despite some progress was achieved in producing nanostructured high strength W/Cu composites, the above-mentioned approaches revealed some drawbacks [2]. Sintering the mechanically alloyed nanoparticles still requires temperatures as high as 900-1000°C, and, therefore results in increasing the grain size greatly [11]. Sintering W/Cu at lower temperatures involves using extra alloying by metallic additives, which are detrimental for both heat and electric conductivities of the composite [2]. Using chemically pure W and Cu particles allows obtaining pure W/Cu composites but the process seems to be energy consuming, multi-stage and tedious [2].

Obtaining the fine-grained composite is feasible with the use of either infiltration or liquid phase sintering. In such a case, the finest W particles may be used but also this may provoke formation of closed pores, which are undesirable from the viewpoint of copper infiltration and obtaining high density. Mechanical and mechano-chemical alloying has been proposed to improve the liquid state sintering but it involves the risk of contaminating the powders.

Spark plasma sintering is a promising process for fabricating W/Cu composites but there is still a problem with obtaining the high-density samples. SPS appears to be an advanced method for producing the W/Cu composites, however, the situation is that the complex relationships between SPS process parameters and final composite characteristics limit the application of this method [2, 12]. Nevertheless, improved densification during the SPS was achieved using bimetallic core-shell particles [2]. Tungsten-rich SPS sintered samples demonstrated high wear resistance and satisfactory electric conductivity [3,4].

HPT allows forming relatively large bulk nanostructured samples as compared to those obtained according to the above-described methods but the grain size distribution is not uniform across the HPTed sample [13].

Alternative approach to avoid the grain growth may be some method of dynamic compaction or sinter forging. Such a method was proposed here to obtain the nanostructured W/Cu composites using a single-pulse magnetic compaction of spherical bimetallic W/Cu particles. These particles, which consist of W and Cu parts joined to form a single particle can be obtained via electric explosion of W and Cu wires (EEW) intertwisted to form a conductor through which a high density ($10^7 \div 10^9$ A/cm^2) current pulse is passed in an argon–filled chamber [14-16]. The result of such an electric explosion is that the solid metals are transformed into fast expanding double-phase homogeneous mixture containing liquid metal clusters and weakly-ionized plasma [17-20]. Such a powder producing process has some advantages over other ones, which also involve physical phenomena. These advantages are as follows: the EEW is a single stage process, no chemical interaction is afforded between the components, W/Cu EEW particles are spherical, and, therefore, can be compacted into fully dense microstructures, high production rate, low energy input, and option to obtain a composite metal/compound particles by changing the buffer gas composition [21].

Magnetic pulse compaction (MPC) is based on transmitting 700 μs duration and 1.5 GPa pressure pulse to a powder load in a mold from a metallic punch accelerated by magnetic field generated by a pulse current from an *RLC*-circuit [14]. Mechanical compaction of particles occurs simultaneously with the adiabatic heating of the powder load, which allows fast sinter forging without increasing the final grain size. The resulting high-density samples are characterized by excess dislocation density due to work-hardening, which may serve for their higher hardness and wear resistance [22-26]. It was shown using numerical modeling [27] that applying a pressure pulse as high as 1 GPa to the homogeneous W/Cu powder mixture it was possible to obtain almost 100% dense composite samples [27]. Considerations and results as above allow understanding that MPC is promising for compacting the bimetallic particles and obtaining the W/Cu nanostructured composites, which then can be characterized and studied.

The objective of this research was to characterize bulk W/Cu composites obtained by MPC from bimetallic W/Cu EEW particles.

2. Material and methods
2.1 Electric explosion of wire (EEW) production of bimetallic W/Cu particles

Bimetallic W/Cu particles were produced by passing high-current pulses generated by an RLC-circuit with parameters $R_c \approx 0.076$ Ω, $L_c \approx 0.78$ μH via a conductor made of two intertwisted W and Cu wires of diameters corresponding to the W-31wt.%Cu composition. When being passed via the conductor these high-current pulses caused its electric explosion (EEW) and atomization in an argon-filled chamber [29]. The weight ratio of metals in the resulting W/Cu powder was determined by the ratio of the masses of tungsten and copper wire equal length portions exploded. The EEW explosion frequency was 0.5 Hz. Production rate for W/Cu bimetallic particles was 138 g/h with electric power consumed at the level of 16.5 kW/(h×kg).

The EEW is a fast-occurring process and main information about electric energy input and phase transitions occurring in the wire during its heating by the passing high-current pulse can be obtained from time dependencies of current and voltage. These dependencies were obtained using the Rogovski coil, ohmic voltage divider and oscilloscope TPS2024b (Tektronix Inc., Beaverton OR, USA) as shown elsewhere [16]. The process parameters corresponding to electric explosion of intertwisted W/Cu wires are given in Table 1.

Table 1. The EEW process parameters for producing W/Cu particles from intertwisted W/Cu wires

Wire	Wire diameter d, mm	Wire length l, mm	Metal yield N, % wt.	Energy of sublimation E_s, J	Capacitor C, mkF	Charging voltage U_0, kV	Buffer gas pressure P, MPa
Cu	0.2	90	31	135	3.2	27	0.3
W	0.2	90	69	153			

The element composition of the W/Cu nanosized particles was examined by energy dispersive spectrometry (EDS) in a transmission electron microscope (TEM) JEOL JEM-2100 (JEOL Ltd., Akishima, Japan)). Particle size distribution was obtained by sedimentation analysis in a disk centrifuge DC24000 (CPS Instruments Inc., Prairieville, LA, USA). Not less than 5.1×10^9 particles were used for reconstructing the size distribution curve.

Powder specimens intended for TEM were prepared by intermixing 80 g of powder with 100 ml ethanol and sonication for 5 min to achieve their deagglomeration. The 10 μL quantity was then sampled and distributed on a carbon-coated $\varnothing$3 mm gold mesh substrate. Samples for 15 min duration sedimentation analysis were prepared by intermixing 40 g of powder with 10 mL of ethanol and sonication for 5 min. Thin foils for TEM were cut off the bulk samples using an electro-discharge machine (EDM), then ground and ion-thinned using a Fishione, Model 1051 TEM Mill machine at accelerating voltage 8 kV at 5° incident angle.

Phase compositions of the powder, consolidated samples and worn surfaces were obtained using an XRD diffractometer Shimadzu XRD-6000 (Shimadzu Corp., Kyoto, Japan).

2.2 Magnetic-pulse consolidation (MPC) of W/Cu particles.

MPC consolidation of the EEW W/Cu particles into bulk samples was carried out using facilities of the Institute of Electrophysics UrO RAN (Yekaterinburg, Russia) [15]. Each sample was obtained by charging 52 ± 0.1 g of the bimetallic powder into a $\varnothing$32 mm mold and then isostatically pre-pressing it until reaching 40% of its theoretical density of 14.16 g/cm^3. Total 15 samples were obtained.

Next stage was heating the sample directly in the mold to 350 ºC and vacuum degassing in a chamber at residual air pressure of 1 Pa for 4h. Electric energy accumulated in a capacitor was then passed via a helical inductor as a breakdown current pulse j, which then created a pulse of magnetic field B in the inductor/concentrator gap to induct the current in concentrator (Fig. 1). Pulse force F was the result of interaction between the induced current and magnetic field and it pushed the concentrator and piston down to compact the powder in the mold.
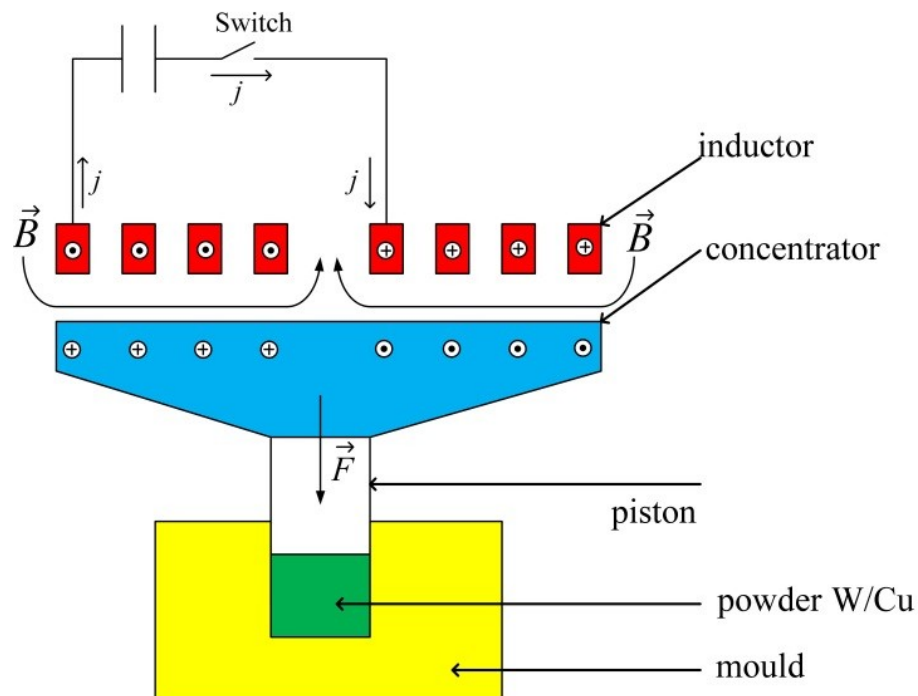

Fig. 1. Schematic diagram of the MPC process [15].

The MPC was performed with the process parameters as follows: electric capacitance (C) ~ 2.2 mF, charging voltage (U_0) ~ 4.1 kV so that the maximum compaction pressure was 1.2 GPa. The pressure pulse rise was 500 μs for all samples. After the MPC, the resulting bulk samples

were annealed without extracting them from the mold at 400 ºC for 2 h to relieve the residual stresses. The resulting samples were 31.3 ± 0.12 mm in diameter and 4.95 ± 0.07 mm in height disks with density in the range 93 to 99% as measured using a hydrostatic weighing method. Electric power consumed for consolidating the bulk sample of total mass 52 g, including stages such as degassing powder, MPC and ensuing tempering for relieving the residual stresses, amounted up to 10.3 kW/h. Total power consumed for W/Cu powder production and consolidation was 11.2 kW/h.

2.3 Mechanical and tribological testing of W/Cu bulk samples.
Specimens for three-point bending tests were EDM cut off the as-sintered disks in the form of $2\times2\times16$ mm^3 bars according to ISO 7438:2020 and tested using a Gotech AI-7000M (Gotech Testing Machines Inc., Taiwan) testing machine at a loading rate of 0.5 mm/min. Total 6 samples were tested. Compression test were carried out on UTS-110M-100-1U (TESTSYSTEMS Ltd., Russia) testing machine using 3x4x6 mm^3 samples at a loading rate of 1 mm/min. Total 6 samples were tested. The Vickers hardness test was performed using a Duramin 400 machine (Stuers A/S, Denmark) at a load of 500 gr with a 10 s dwell time.
High-temperature tribological pin-on-disk testing of the samples was carried out using a nanotribometer THT-S-BE-0000 (CSM Instruments, Peseux, Switzerland) with experimental conditions as shown in Table 2.

Table2. Tribological experiment conditions

N	Temperature, °C	Acquisition rate, Hz	Radius, mm	Time, s	Linear Speed, m/s	Normal Load, N
1	25					3
2	100					3
3	250	200	8	3600	0.4	3
4	350					2
5	450					2
6	550					2

3. Results and discussion.
3.1 Phases and size distribution of W/Cu powder
Time dependencies of currents and voltages were in-situ recorded during EEW of W/Cu wires (Fig. 2). The voltage $U(t)$ curve showed the presence of two maxima at $t \sim 1.29$ μs and $t \sim 1.57$ μs, which corresponded to the explosion of copper and tungsten wires, respectively. The energy $E(t)$ dependencies demonstrated that the energy inputs in copper and tungsten wires achieved values of $2.4 \cdot E_{s(Cu)}$ and $0.9 \cdot E_{s(W)}$, respectively, by the moment of time $t \sim 2.25$ μs when an arc discharge happened. It is known [18,19] that the phase state of the explosion products is determined by the energy input. In particular, the energy inputs in the range $1.5 < E/E_s < 3.0$ into silver, copper or aluminum wires allow generating a homogeneous mixture of weakly ionized plasma and liquid metal nanosized clusters. At the same time, input of $\sim 0.9 \cdot E_s$ energy into a tungsten wire results in explosion formation of micron- and submicron droplets [19, 20].
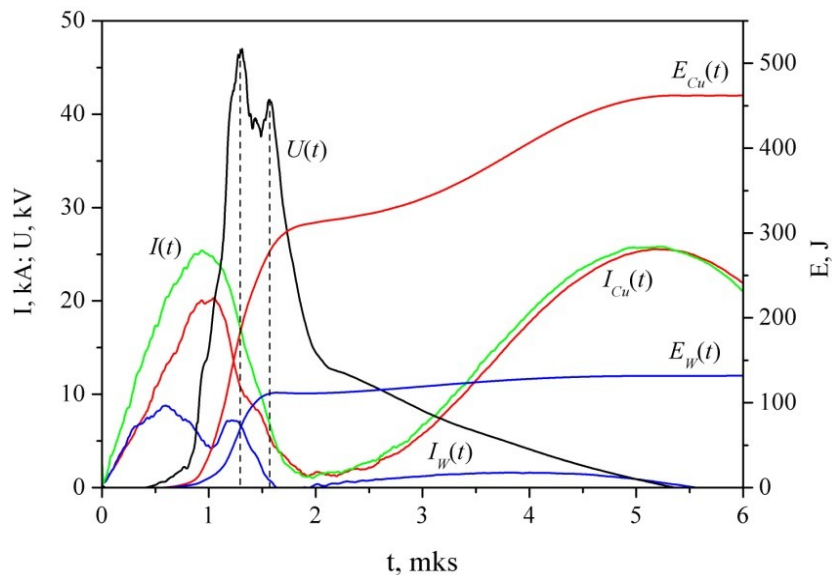
Fig.2. Time dependencies of currents and voltages *in-situ* obtained during EEW of W/Cu intertwisted wires.

A SEM micrograph of W/Cu particles (Fig.3a) shows, as expected from the above analysis, the presence of both nano- and micron-sized particles in the explosion products. Explosion of a tungsten wire produced micron-submicron tungsten droplets, which then solidified into the same size particles, while because of the high E/E_s ratio the copper wire explosion gave only few micron-sized copper droplets with the majority of the submicron size ones. The W/Cu particle size distribution curve in Fig.3b reveals two local maxima that may be related to action of different particle forming mechanisms: (i) liquid droplet dispersion and (ii) coagulation/coalescence of the vapor clusters.
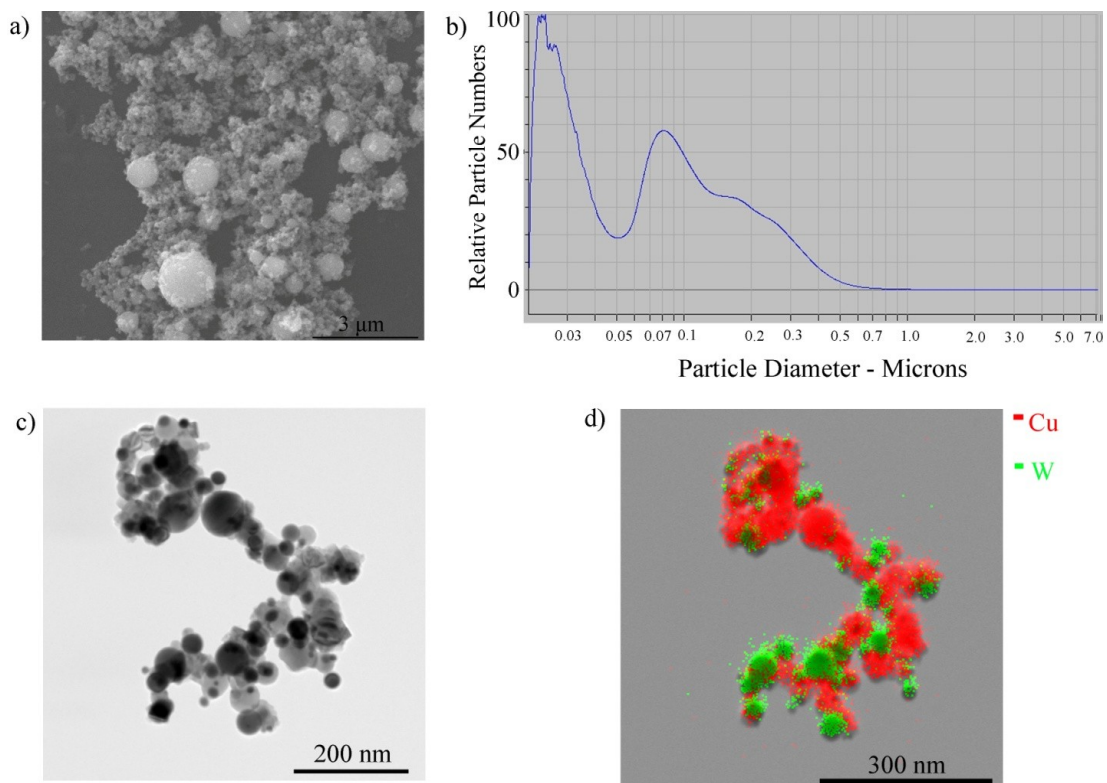

Fig.3 Characteristics of the obtained EEW powders: (a) SEM micrograph, (b) particle size distribution, (c) TEM micrograph and (d) EDS mapping of W/Cu nanoparticles.

The EDS map of element distribution in the particles (Fig. 3c, d) shows that the nanosized particles are spherical and mainly composed of a single metal. This finding differs from that of previous reports on bimetallic particles obtained by EEW of intertwisted wires of partially and fully miscible metals, other than W and Cu. The EEW of intertwisted wires of partially miscible metals usually gave nanosized "core-shell" or "Janus-like" particles formed by metal segregation within such a particle as a result of coalescence/coagulation of dissimilar metal clusters [29, 30]. In the case of W and Cu particles, another type of bimetallic particles is formed by diffusion bonding of W/Cu at temperatures close to the copper melting point. It was shown [31] that a mutual diffusion layer of 20 nm thickness could be formed between these metals.

The W-Cu binary system is characterized by the enthalpy of formation 33 kJ/mole [32]. It means that the energy barrier for formation of bimetallic W/Cu nanoparticles by spontaneous coalescence of clusters is too high [33]. Solidification of these particles from a binary melt is also hardly possible because melting point of tungsten is well above the boiling point of copper. Summarizing all the above-discussed facts we suggest that possible mechanism for the formation of the W/Cu bimetallic particles lies with intermixing and collision of single-metal particles with some diffusion bonding.

An X-ray diffractogram obtained from the W/Cu powder showed phases such as BCC α-W, Cr_3Si–type A15 β-W and FCC Cu (Fig. 4). The lattice constants of both α-W and Cu were close to their standard values.

The presence of the metastable, brittle and poor conducting β-W phase in bimetallic particles is typical with the EEW production of tungsten powders [21] and may be related to nonequilibrium condition of the process. According to the XRD data, the weight percentage ratio of α/β phases of tungsten in the sample was 16/53. According to the literature sources, β-W phase has a higher electrical resistivity (150–300 μΩ-cm), in comparison with α-W phase (5.3 μΩ-cm), and a sample based on α + β phases has a significantly lower strength (780 MPa) vs. that of the α-W phase one (1480 MPa) [35-38].This β-W phase is usually obtained as thin films in such processes as magnetron sputtering [39]. One of the factors behind the α→β transformation may be the presence of oxygen [40]. At least, the inverse β→α transformation may be achieved either by removal of oxygen or due to heating to 520 ^{0}C [41, 42]. High cooling rate also can be a stabilizing factor for the β-W phase. It is known [43] that cooling rates in the order of ~ $10^7 \div 10^9$ K/s can be achieved in solidification of nanoparticles produced via EEW and therefore serve for stabilizing the β-W.
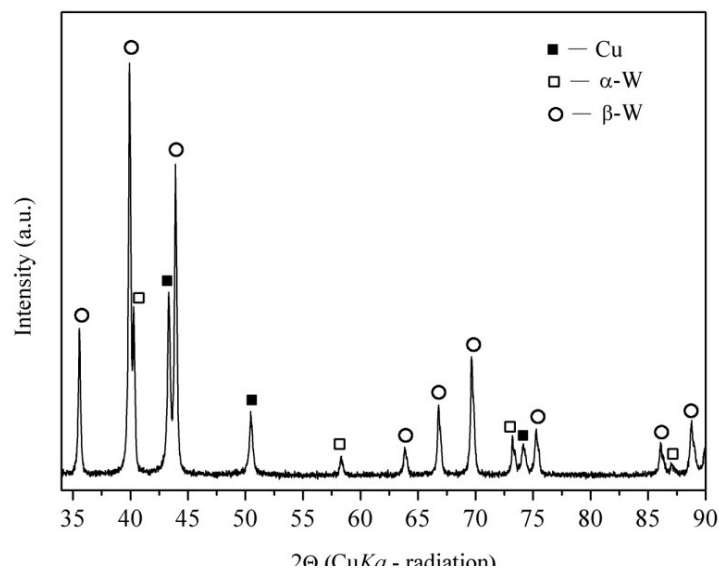

Fig. 4 The XRD diffractogram obtained from the W/Cu powder.

3.2 Phases and microstructures of consolidated W/Cu samples

The XRD pattern of MPCed samples showed the presence of α-W, β-W and Cu phases inherited from the source powder as well as tungsten dioxide WO_2 that resulted from oxidizing during the compaction in air (Fig.5).
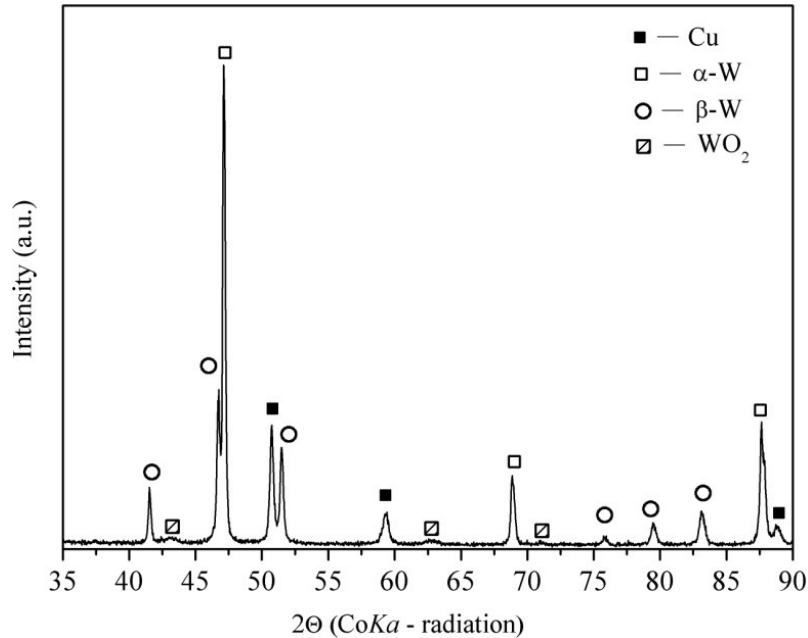

Fig.5. The XRD diffractogram obtained from bulk magnetic pulse compacted W/Cu samples.

SEM BSE image (Fig.6a) and corresponding EDS maps (Fig.6b, c) allow observing that the MPCed sample's microstructure is composed of a copper matrix with more or less uniformly distributed micro- and submicron-sized spherical tungsten particles. Since volume percentage W/Cu ratio is about 50/50 and great part of the W total mass is represented by these particles then, when specifying the MPC regime parameters (temperature and pressure), we were orienting on those used for consolidation of copper nanoparticles [14]. The resulting density values for MPCed WCu samples, namely in the range 93 ÷ 99% were in good agreement with 95% for those obtained on the MPCed copper [14].
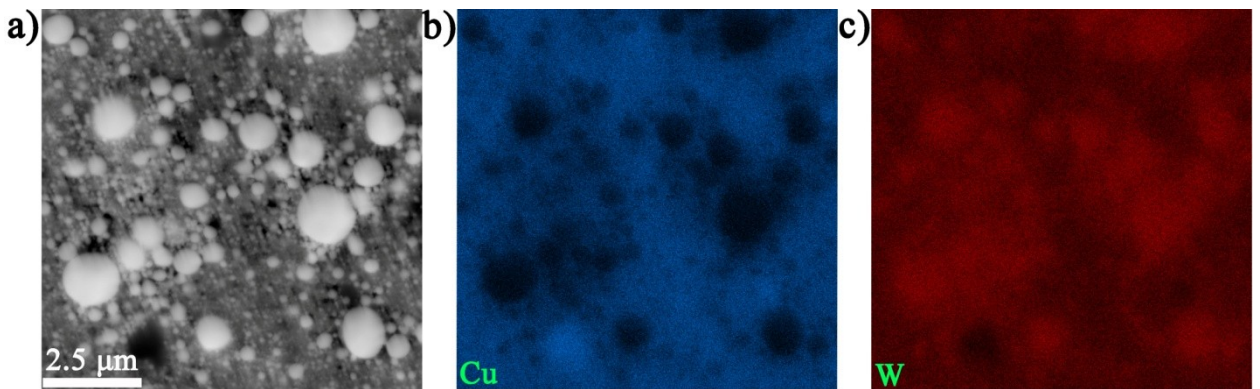

Fig.6. SEM BSE image (a), EDS copper (b) and tungsten distribution (c) in a magnetic-pulse consolidated W/Cu sample

TEM images obtained from thin foils (Fig.7a, e) demonstrated sub-micron tungsten spherical particles in the copper matrix with fine recrystallized 59 ± 3 nm grains, featuring grain boundaries and annealing twins. Selected area electron diffraction pattern (SAED) in Fig.7c and its indexed image in Fig 7d show the same phases as those identified from the XRD (Fig. 5), i.e. α-W, β-W, Cu as well as monoclinic WO_2. According to XRD data weight percentage ratio of the α/β phases of tungsten in the bulk magnetic pulse compacted was 58/11, respectively.

The microstructure of the consolidated samples showed that copper grains (Fig.7b) were formed by solid state sintering of copper particles without full fusion. Tungsten particles were not fully wetted by copper and, therefore, there were voids and pores especially around the coarser particles (Fig. 7e-g). We believe that, unless the magnetic pulse consolidation was used for the bimetallic W/Cu particles, no bonding would have been achieved between the tungsten particles and copper matrix. The other positive outcome was that the copper matrix grains were very fine as well as additionally contained annealing twin high-angle boundaries, which served as effective dislocation barriers and contribute to the Hall-Petch strengthening during mechanical loading.

The relative density values in the range 93 to 99% that were obtained on the magnetic pulse consolidated samples are in agreement with the results obtained from numerical modeling of W/Cu spherical particle compaction [27]. It was established that the relative density of compacted EEW powders of composition 69 wt.% W-31 wt.% Cu, which is equal to volume percentage ratio W/Cu 50/50 [5] was 0.95 for the compaction pressure as high as 1.2 GPa.

Von Mises microstress distribution was reconstructed to show that the presence of W-based particle agglomerates had a great effect on the residual porosity. It was reported [27] that these agglomerates required applying higher force for their full compaction. Such a conclusion is in agreement with the experimental data shown in Fig.7e.

The maximum residual porosity was observed in regions close to coarse W particles. Therefore, in addition to the increasing the compaction pressure, porosity in MPC can be further reduced by improving the particle size uniformity. The W/Cu size distribution uniformity may be provided by increasing the energy input into wires and thus refining the W particles. It was shown [44] that mean W particle sizes obtained using EEW regimes with arc discharge by the explosion products in argon, nitrogen and helium atmospheres were in the range 13 to 21 nm, i.e. both submicron and micron-sized droplets were evaporated by the discharge. Even full transformation of a W-wire into a plasma gas state can be achieved during the EEW under condition of corresponding modification of discharge circuit and electric field [45]. Therefore, minimization of coarse micron-sized W-particle content and improved particle size uniformity can be achieved in EEW. It should be noted also that increasing the energy input at the arc discharge stage may also increase the mean particle size by forming tough particle agglomerates. These agglomerates will interfere with the powder flow during MPC and, therefore, should be avoided.
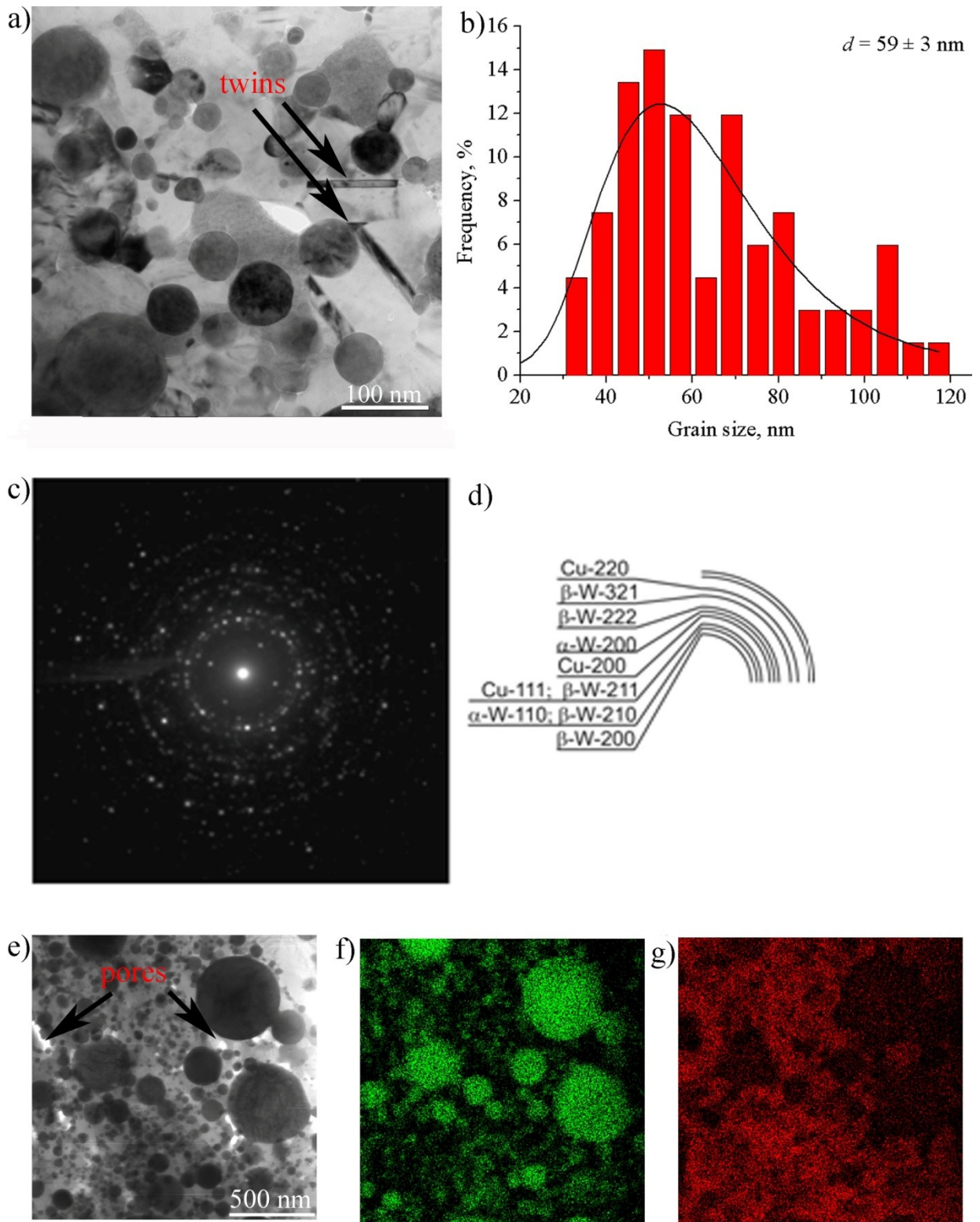
Fig.7 TEM images (a, e), grain sizes distribution (b), (c) SAED pattern, (d) SAED pattern indexed and EDS maps (f(W), g(Cu)) of magnetic-pulse consolidated W/Cu samples.

3.3 Mechanical characteristics of consolidated W/Cu samples

All as-consolidated W/Cu samples were bent until full fracture and mean flexural strength was determined at the level of 560 ± 10 MPa. Fracture occurred just after reaching the ultimate flexural strength but according to stress-strain diagram in Fig. 8a samples experienced plastic deformation from the very beginning of the test. More support for such an observation can be seen from analyzing the stages on a stress derivative σ'_ε vs. strain curve in Fig. 8b.
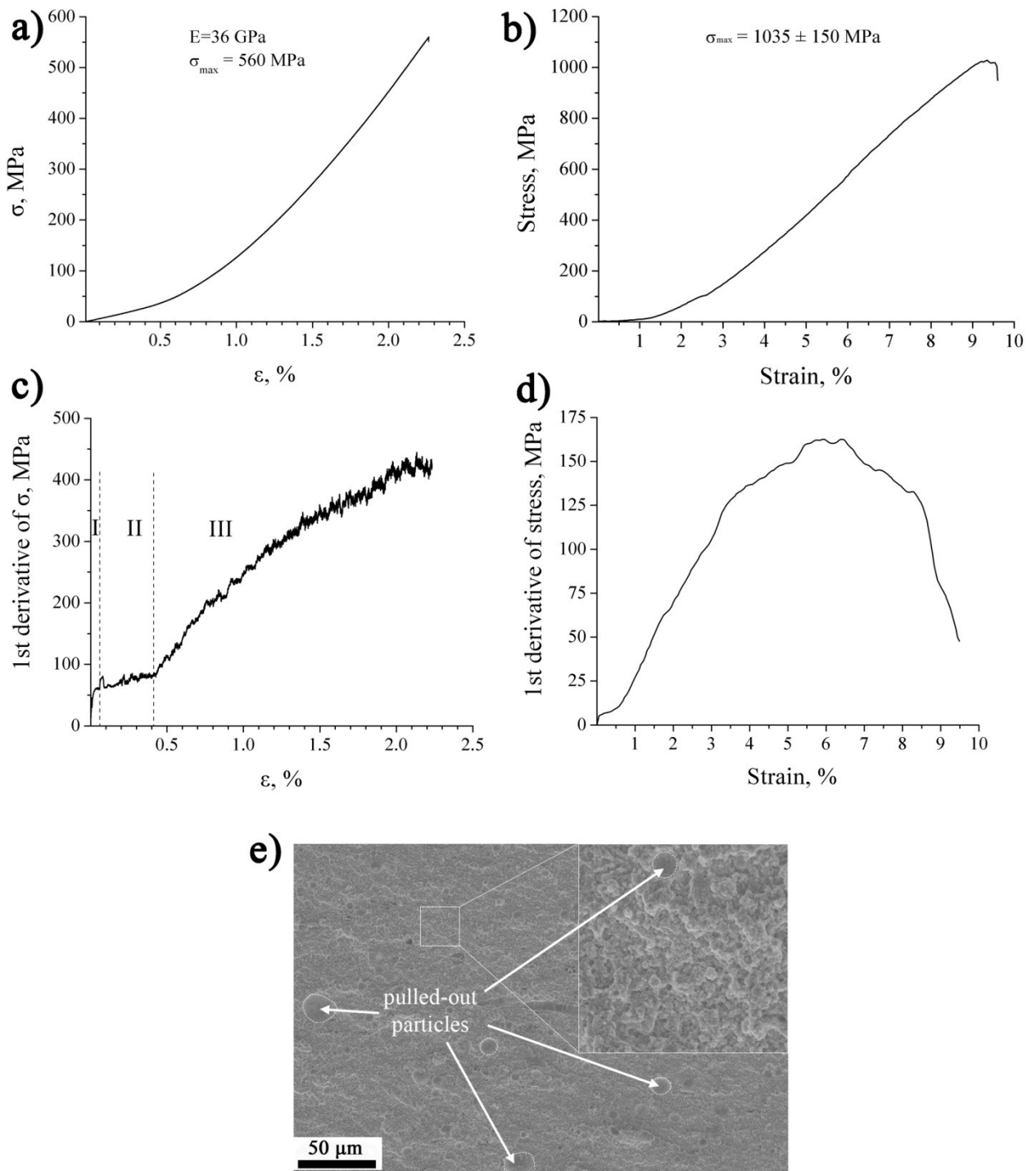
Fig. 8. Bending (a, b) and compression (d, e) test stress-strain curve (a, d), 1st derivative of stress vs. strain curve (b, e), fracture surface (c) of W-Cu bulk samples

Stage I corresponds to sharp non-linear growth of stress while stage II demonstrates moderate almost linear strengthening. Stage III corresponds to non-linear strengthening until complete fracture. Non-linear behavior of strengthening factor σ'_ε at the stage I can be the result of friction between the sample and supports. Low rate strengthening at stage II can be related with microfracture and pore collapse. Stage III non-linear strengthening may be the result of Hall-Petch hardening in the nanostructured copper matrix. Nevertheless, the resulting fracture surfaces can be characterized as ductile with dimples and voids formed due to pulling out coarse tungsten particles only weakly bonded to the copper matrix (Fig. 8c).

The behavior of specimens during compression tests was characterized by accumulation of cracks while retaining the sample's integrity and final fragmentation at the last stage. Thus, the

common fracture pattern can be defined as a viscous-plastic one. The onset of crack formation is observed at about 5-6% strain, which is most clearly seen on the strengthening factor curve (Fig. 8e). The compression curve (Fig. 8d) contains the "positive bending - slope - negative bending" parts, common for the compression test. A critical fracture occurs after achieving the 9% strain when the curve first reaches a plateau and then abruptly breaks off. In this area, there is an intensive growth of cracks and the beginning of partial cleavage. Compression tests showed that ultimate compression strength (UCS) was at the level of 1035 ± 150 MPa for all samples independently of the compression axis orientation with respect to the compaction force direction. The mean hardness number was 317 ± 1 HV.

The compression strength was by a factor of 1.8 higher than the flexural strength. It should be noted that for both copper and tungsten the differences between flexural and compression strengths are not that big [46]. The observed difference might have resulted not only from the test and sample geometry differences but also from structural inhomogeneity of the MPC sample. The presence of defects such as pores and lack of bonding between copper and tungsten can be factors behind the low flexural strength.

Table 3 contains characteristics of bulk consolidated W-30 wt/ % Cu samples obtained according to different methods. One can see that the MPCed samples have density values close to those obtained using other methods.

Table 3. Characteristics of bulk consolidated W-30 wt/ % Cu samples obtained according to different methods.

Preparation of powder	Sintering	Grain size, μm	Relative density, %	Hardness	Electrical conductivity	Ref.
exploding wire	magnetic pulse compaction	0.02-3.0	93-99	317 HV	—	this work
mixing, milling, coating	spark plasma sintering, vacuum sintering	0.2-5.0	88-90	2.33-3.11 GPa	$(2.78\text{-}4.93) \times 10^6\ \Omega^{-1}\text{m}^{-1}$	[6]
blend	infiltration	micron	98.9	178 HB	39.32 % IACS	[1]
blend	infiltration	0.4	98.7	194 HB	41.03 % IACS	[1]
sol-gel	field assisted	0.35-0.4	97.3	—	—	[1]
spray-drying	liquid-sintering	submicron	99.0	—	—	[1]

3.4 Tribological behavior of consolidated W/Cu samples

Time dependencies of the coefficient of friction (CoF) in Fig. 9 showed that the CoF magnitude stabilized after some short period of time. The highest CoF was demonstrated during sliding at 100°C which even had a tendency to grow with the time. The minimum CoF values were obtained in sliding at 250°C, 350°C, and 450°C (Fig. 9). Sliding at 550°C showed somewhat higher friction but still below those obtained at 100°C and even 25°C.
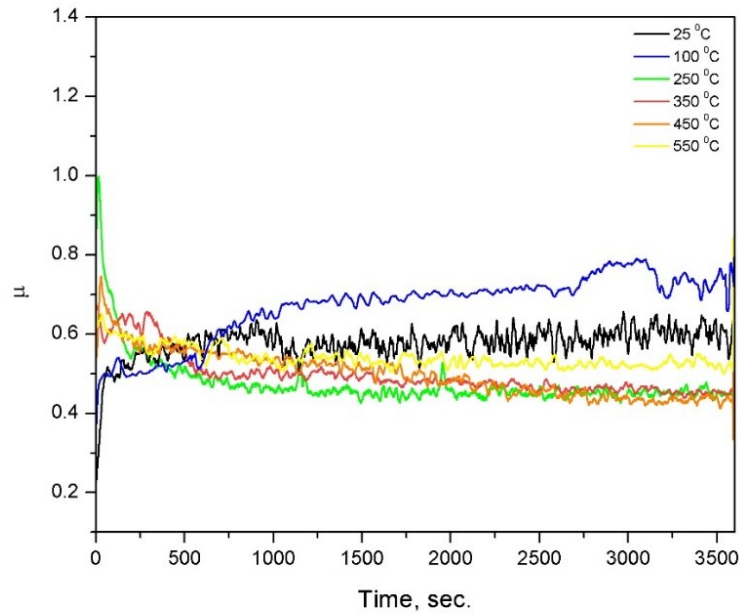
Fig.9. Time dependencies of the coefficient of friction for W-Cu composite samples tested at different temperatures
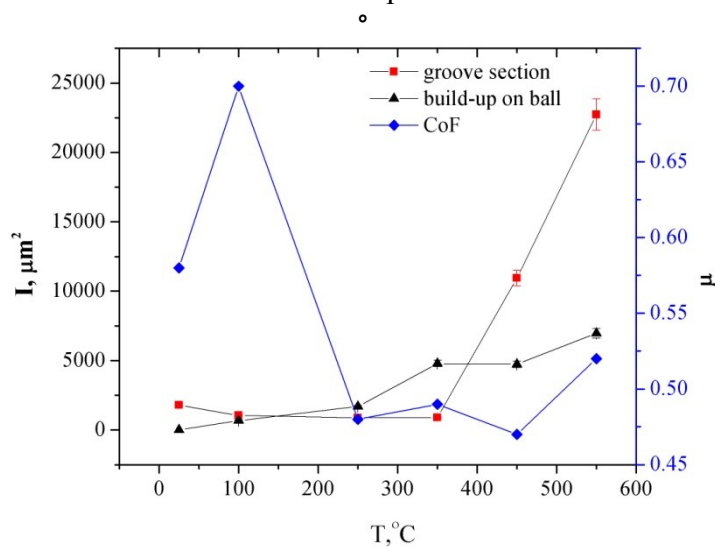

Fig.10. Temperature dependencies of the wear and friction coefficients of the W-Cu consolidated samples and steel balls

Wear behavior of MPC W/Cu samples slid against ASTM 52100 steel balls (Fig. 10 and Fig. 11) allow suggesting that the wear groove cross section area was almost constant at the test temperatures 25°C-350°C and increased sharply at 450°C and 550°C.

The loss of material by wear might occur due to removal of metal from the wear contact or by transfer of metal to the counterbody. Therefore, the worn surfaces of the steel balls were examined too. Intense wear of balls occurred during sliding at 25°C and 100°C (Fig. 12) so that the ball surface was flattened and, plausibly, the steel wear debris were removed or transferred to the W/Cu sample worn surface. Starting from 100°C there were build-up zones whose cross section area increased with the temperature by means of inverse adhesion transfer of W/Cu onto the steel ball surface. The most intense transfer of W/Cu on the steel ball occurred at 450 and 550°C (Figs. 10, 11, 12).
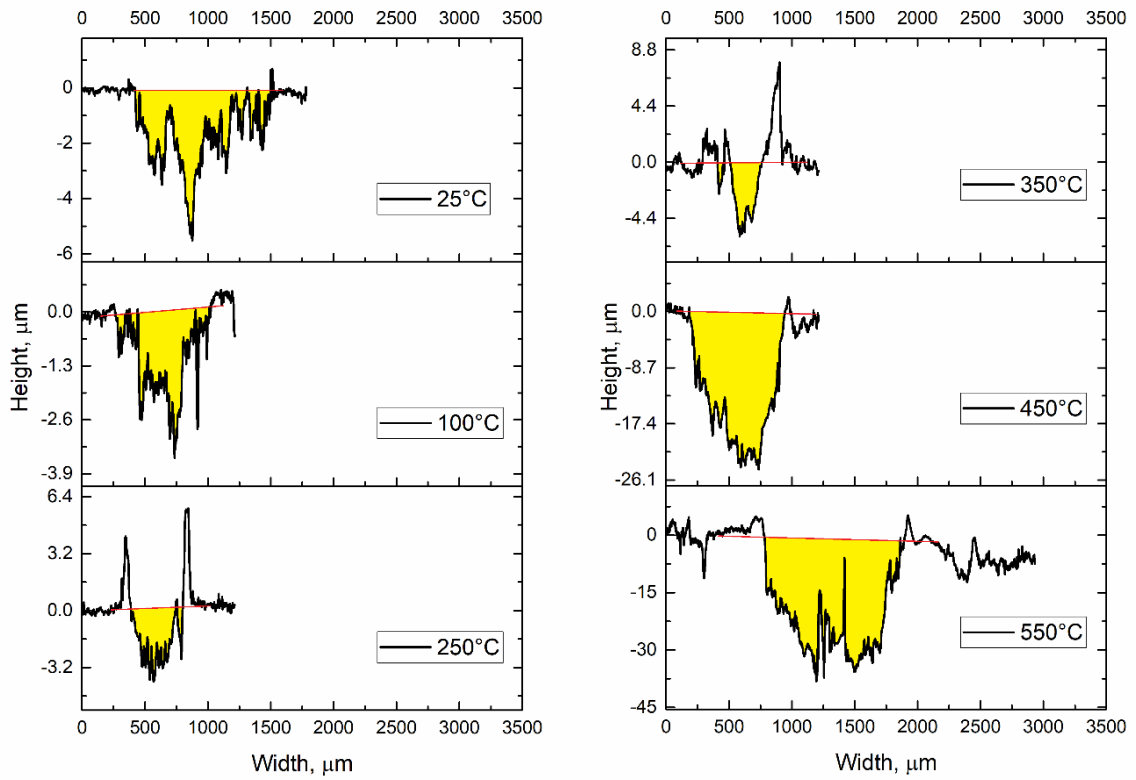
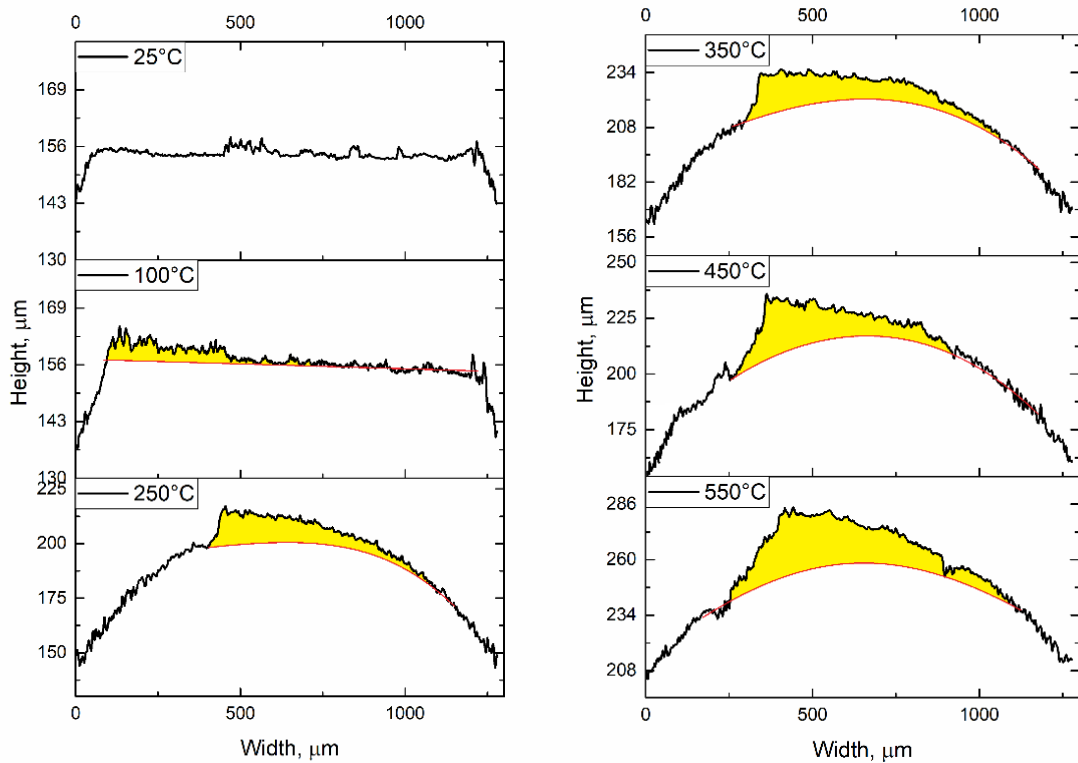Fig. 11. Wear track profiles on the disk surfaces.

Fig.12. Tribological transfer layer on the ball surfaces.

SEM images of the worn surfaces in Fig. 13 show adhesion wear morphology of samples tested at 25 and 100°C. Starting from 250°C, transfer (mechanically mixed) layer covered areas (TLA) appear that bear contact loads and reduce friction. This temperature is the wear transition

point where the adhesion wear of steel ball is substituted for the adhesion wear and transfer of W/Cu samples. Along with these TLA there are transfer-layer free areas (TLFA) which appear to form by detachment and removal of the TLA.
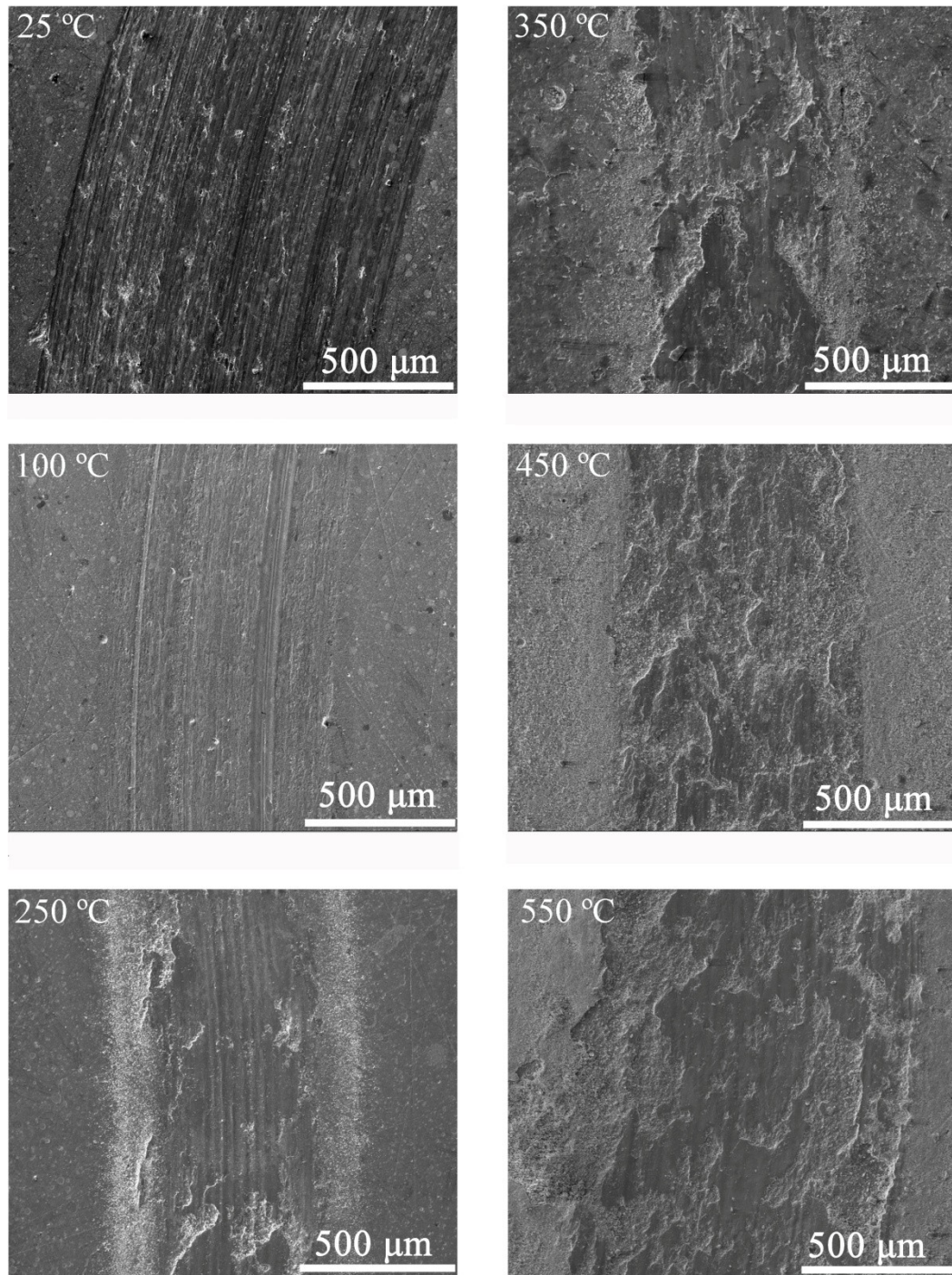

Fig.13 SEM BSE images of worn surfaces on the W/Cu MPCed samples obtained at different test temperatures.

3.4 XRD and EDS element distribution after wear
X-ray diffractograms were obtained from the worn surfaces (Fig.14a) and compared to those from free W/Cu sample surface (Fig.14b). The worn surfaces of samples tested at 25°C and 100°C revealed the presence of the same phases as those found in as-compacted samples and on the unworn areas of the samples, i.e. α-W, β-W, Cu, and WO_2. The differences started at 250°C when the unworn surface showed copper oxides Cu_2O, CuO. At the same time, the worn surfaces

were even more heavily oxidized and revealed copper tungstate $CuWO_4$ in addition to CuO. The amount of $CuWO_4$ on the worn surfaces of W/Cu samples became higher at 450°C and 550°C and, in addition, there appeared reflections of tungsten trioxide WO_3. On the unworn surface, the reflections of $CuWO_4$ were detected only after heating to 550°C (Fig.14a). It should be noted that β-W reflections disappeared from both types of surfaces starting from 450°C, i.e. at the temperature lower than 520°C [42]. It seems that severe plastic deformation on the worn surface facilitated the β→α transformation despite intense tribooxidizing.
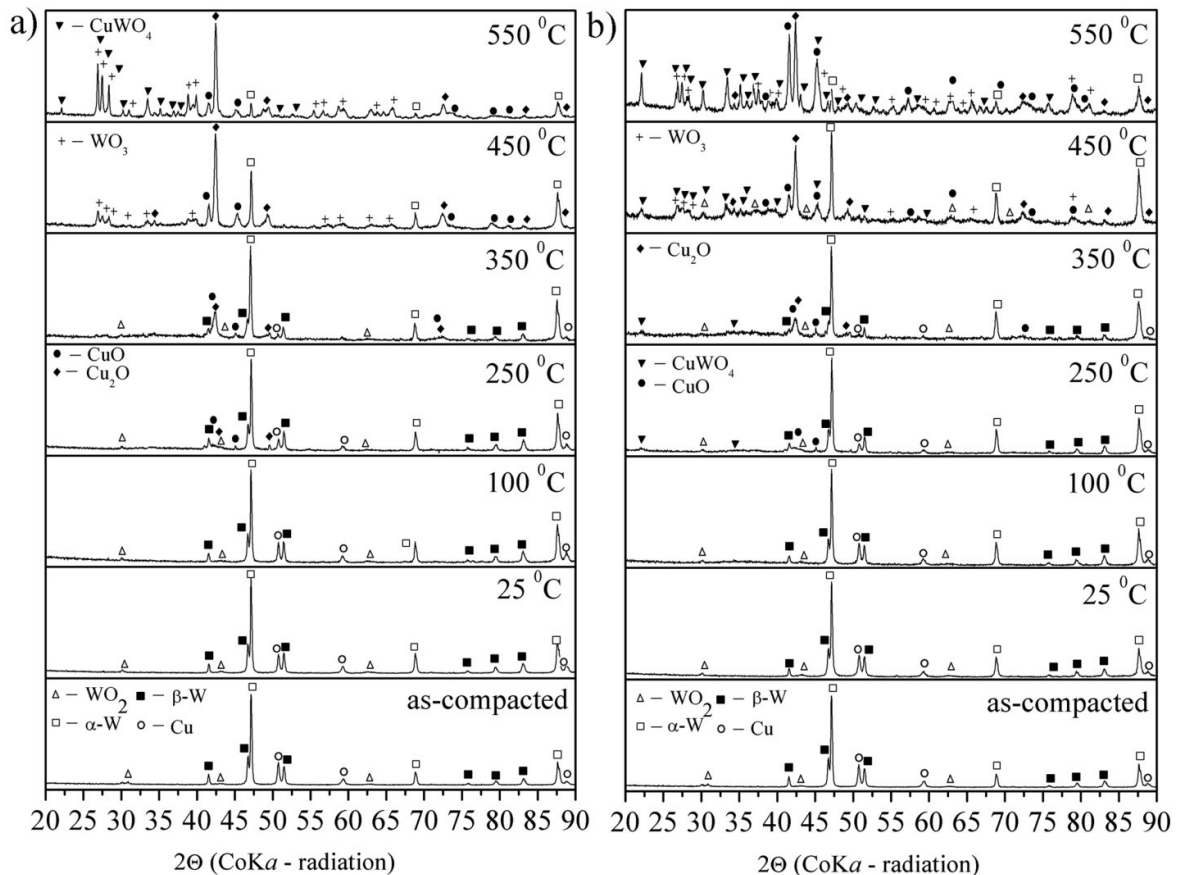
Fig.14. XRD spectra obtained from (a) unworn and (b) worn surface areas of W/Cu samples tested at temperatures as shown.

SEM examination of the worn surfaces revealed thin needle-like WO_3 crystals, which grew after stopping the tests upon cooling the sample in air (Fig.15). No free copper was detected on the worn surfaces of samples tested at high temperatures owing to fact that all copper was spent for generation of copper tungstate.
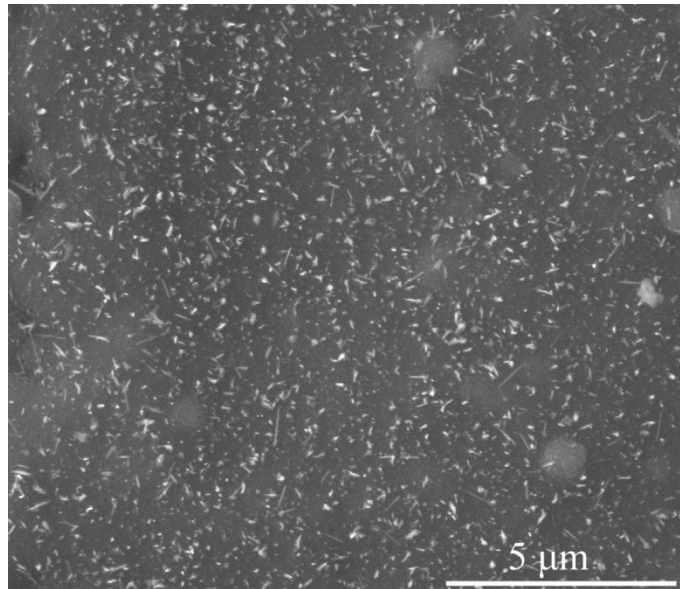
Fig.15. SEM BSE image of fine WO_3 crystallites grown on the worn surface of a sample tested at 550°C during cooling in air.

The EDS mapping of the worn surfaces demonstrate how both tungsten and copper reduced their concentrations during sliding at 25°C and 100°C (Fig.16). Then tungsten concentrations further reduced as the sliding temperature grew, while that of copper started grow being below its concentration in the as-compacted material. Moderate concentrations of iron were detected on the worn surfaces of samples tested at 25°C and 100°C, which testified to the transfer from the steel ball. The intensity of the iron transfer reduced in sliding at higher temperatures when inverse transfer process activated. The increasing with temperature concentration of oxygen is an expected effect since the higher the temperature, the more intense the oxidizing.
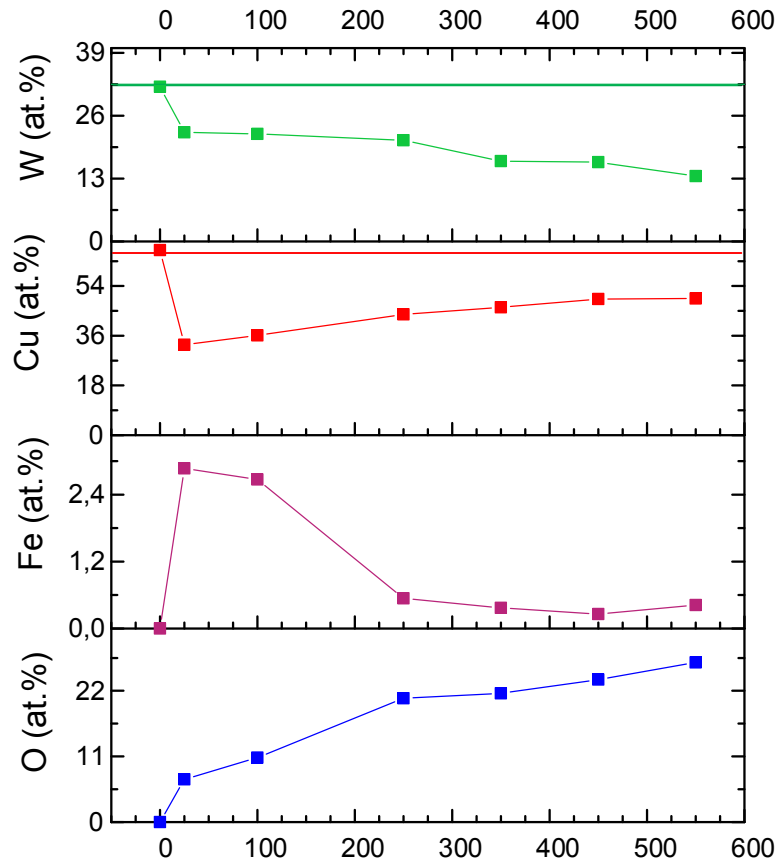
Fig.16 Wear surface composition vs. test temperature (0 corresponds to the as-compacted material). Horizontal lines mark up the initial concentrations of corresponding elements in the W/Cu composite.

More detailed EDS examination of the worn surfaces confirmed the observations as made above. Almost nothing happened to W and Cu concentrations after sliding at 25 °C and 100°C except for some oxidizing (Fig.17). At 250°C, 350°C and 450°C there were some drops in copper concentration across the wear groove with simultaneous enrichment by tungsten. It should be noted that TLA were enriched with W while TLFA were enriched by copper. It seems that TLA represents the mechanically mixed material composed of copper tungstate and other oxides while composition of TLFA is closer to that of as-compacted material. Such a finding may be a strong point in favor of TLFA formation by removal of TLA.
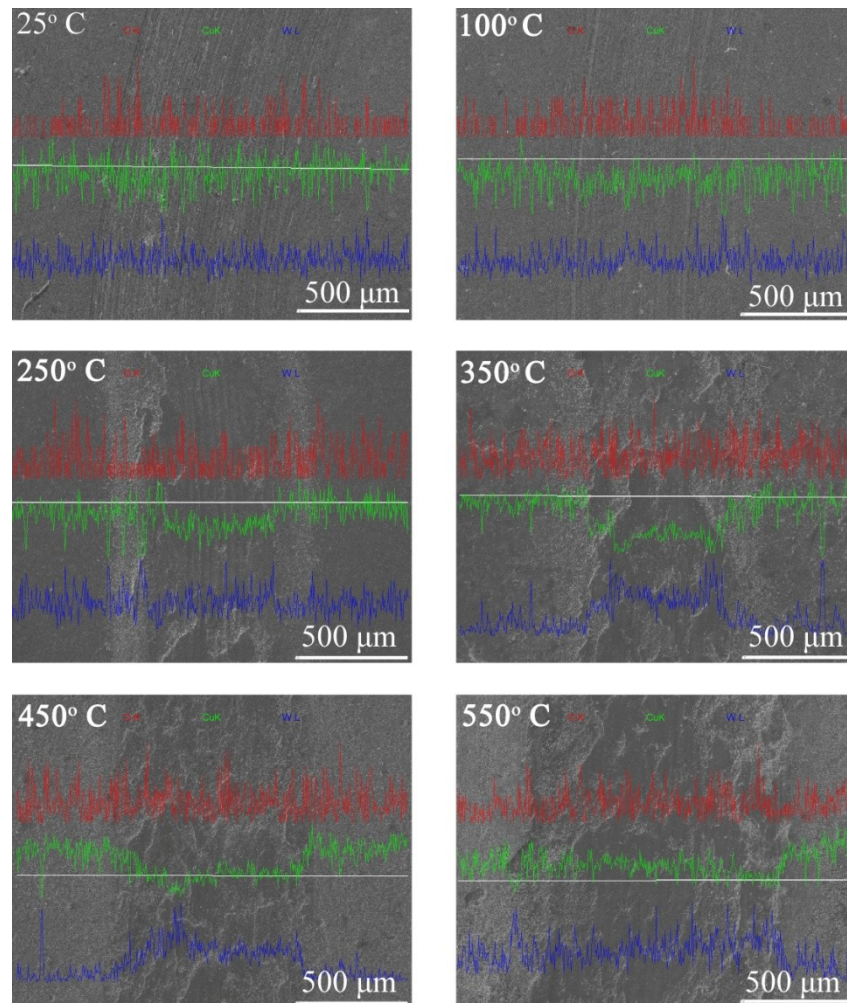
Fig.17. EDS spectra of the wear grooves on W/Cu samples after sliding against steel balls at different temperatures

Tribological testing of W/Cu consolidated bulks showed at least three stages depending on the test temperature. The first stage was characterized by a special type of the worn surface with asperities manifested as multiple narrow grooves on both surfaces, which appeared because of scratching and ploughing them by hard phases. These hard particles may represent tungsten particles pulled out as some of those were only weakly bonded to the copper matrix because of partial sintering. At 25-100°C testing temperature there was no strong adhesion and transfer between the steel ball and W/Cu composite. Both surfaces were worn and oxidized uniformly and wear debris were removed from the contact zone to the periphery. There was no pile-ups on the wear track edges, which could evidence plastic deformation. Tribooxidation of all components such as tungsten, copper and iron mainly occurred in wear particles so that scratching and ploughing happened on the non-oxidized surfaces. That is why the CoF values are very high at 25 and 100°C, namely, ~0.57 and ~0.7, respectively (Fig. 9). It is interesting that adhesion transfer onto the steel ball was zero in sliding at 25°C and non-zero at 100°C. Therefore, friction was higher in the latter case.

The worn surfaces of samples tested at temperatures 250°C and 350°C resulted in generation of smooth TLA areas covered with mechanical mixed layer (MML) and rough (TLFA) areas formed by detachment and removal of the MML. Intense tribooxidation and mechanical mixing at these temperatures produced copper tungstate, which proved to be an adaptation factor for reducing both friction and wear despite intense adhesion transfer onto the steel ball.

There were high pile-ups on the wear track edges testifying to the plastic edging of W/Cu as well as plasticization and deformation of coarse tungsten particles, which then smeared over

the surface and oxidized (Fig.11, Fig.17). Such a redistribution resulted in enrichment of the wear track surface with tungsten.

Adhesion transfer of mechanically mixed layer (MML) onto the steel ball surface intensified but the anti-friction effect of in-situ formed copper tungstate extended to 450°C and even 550°C. However, thermal softening of the W/Cu composite matrix eventually became too great, which resulted in the significant increase of the wear track depth.

These analysis fits the conception of structural–energetic tribological adaptation of materials to sliding conditions first proposed by B.I. Kostetsky [47]. Interest to studying all kinds of effects observed with such an adaptation on different materials is now reviving, especially, in view of testing new interesting and promising materials such as MAX-phases, high-entropy alloys and carbides, ultra-high temperature ceramics, etc.

One of the effective adaptation ways may be formation of mixed oxides capable of easy shear [48]. For example, copper spinel was the reason for friction reduction upon sliding on a compacted Fe/Cu pseudoalloy [25]. Tungsten is also known as a metal capable of forming soft oxides like tungsten trioxide and Magneli phases [49] that may serve as solid lubricants [50, 51]. Mixed oxides – tungstates may in-situ form during high-temperature (high-speed) sliding and then reduce friction [52]. Friction reduction effect of in-situ $CuWO_4$ in sliding test on W/Cu composite at 900°C was reported [53]. Our results and analysis agree well with this concept and we demonstrated that the formation of oxides in the studied W/Cu composite plays important role in its tribological behavior.

4. Conclusion

The novelty of this study is in consolidating bespoke bimetallic core-shell W/Cu nanoparticles with magnetic pulse sintering that combines consolidating with severe plastic deformation. Bimetallic W/Cu particles were obtained using electric explosion of intertwisted wires in argon-filled chamber. Particle size distribution was bimodal in accordance to the phase state specifics of the explosion products. The EEW particles contained phases such as Cu, α-W and β-W. The samples compacted by magnetic pulse (MPC) had 93-99% density and additionally contained WO_2 formed as a result of oxidation in compaction. Microstructurally the MPC samples were composed of copper grain matrix, pores and tungsten particles. Flexural and compression strengths were 560 ± 10 and 1035 ± 150 MPa, respectively. The MPC sample strength can be improved using more uniform particle size distribution and elimination of the coarse micron- and submicron-sized tungsten particles.

Coarse tungsten particles were only weakly bonded with the matrix and, therefore, were pulled out during sliding test at low temperatures and abraded the worn surfaces.

Formation of copper tungstate in tribooxidation at 250°C-350°C allowed reducing both the wear and the friction. At even higher temperatures of 450 to 550°C, copper tungstate still works beneficially, but thermal softening of the copper matrix is too great and so that W/Cu is ploughed deeply by the steel ball with the strong build-up.

References

1. C. Hou, X. Song, F. Tang, Y. Li, L. Cao, J. Wang, et al., W–Cu composites with submicron- and nanostructures: progress and challenges, NPG Asia Mater. 11 (2019) 74. https://doi.org/10.1038/s41427-019-0179-x

2. Y. Wang, L. Zhuo, E. Yin, Progress, challenges and potentials/trends of tungsten-copper (W-Cu) composites/pseudo-alloys: Fabrication, regulation and application, Int. J. Refract. Met. Hard Mater. 100 (2021) 105648. https://doi.org/10.1016/j.ijrmhm.2021.105648

3. J.K. Liu, K.F. Wang, K.C. Chou, G.H. Zhang, Fabrication of ultrafine W-Cu composite powders and its sintering behavior, J. Mater. Res. Technol. 9 (2020) 2154-2163. https://doi.org/10.1016/j.jmrt.2019.12.046

4. L. Cao, C. Hou, F. Tang, T. Han, X. Huang, Y. Li, et al., Wear-resistance enhancement of nanostructured W-Cu-Cr composites, Int. J. Refract. Met. Hard Mater. 101 (2021) 105673. https://doi.org/10.1016/j.ijrmhm.2021.105673

5. Y. Li, C. Hou, L. Cao, C. Liu, S. Liang, F. Tang, et al., Excellent wear resistance of multicomponent nanocrystalline W–Cu based composite, J. Alloys Compd. 861 (2021) 158627. https://doi.org/10.1016/j.jallcom.2021.158627

6. A. Elsayed, W. Li, O.A. El Kady, W.M. Daoush, E.A. Olevsky, et al., Experimental investigations on the synthesis of W-Cu nanocomposite through spark plasma sintering. J. Alloys Compd., 639 (2015) 373-380. https://doi.org/10.1016/j.jallcom.2015.03.183.

7. V. Madhur, M. Srikanth, A.R. Annamalai, A. Muthuchamy, D.K. Agrawal, C. Jen, Effect of nano copper on the densification of spark plasma sintered W-Cu composites, Nanomaterials. 11 (2021) 413. https://doi.org/10.3390/nano11020413.

8. I. Sabirov, R. Pippan, Formation of a W-25%Cu nanocomposite during high pressure torsion, Scr. Mater., 52 (2005) 1293-1298. https://doi.org/10.1016/j.scriptamat.2005.02.017

9. D. Edwards, I. Sabirov, W. Sigle, R. Pippan. Microstructure and thermostability of a W-Cu nanocomposite produced via high-pressure torsion. Philos. Mag., 92 (2012) 4151-4166. https://doi.org/10.1080/14786435.2012.704426

10. M. Rosalie, P. Ghosh, J. Guo, O. Renk, Z. Zhang. Microstructural and texture evolution of copper-(chromium, molybdenum, tungsten) composites deformed by high-pressure-torsion. Int. J. Refract. Met. Hard Mater., 75 (2018) 137-146. https://doi.org/10.1016/j.ijrmhm.2018.04.008.

11. J.C. Kim, I.H. Moon, Sintering of nanostructured W-Cu alloys prepared by mechanical alloying. Nanostruct. Mater., 10 (1998) 283-290. https://doi.org/10.1016/S0965-9773(98)00065-8

12. Z.Y. Hu, Z.H. Zang, X.W. Cheng, F.C. Wang, Y.F. Zhang, S.L. Li, A review of multi-physical fields induced phenomena and effects in spark plasma sintering: Fundamentals and application, Mater. Design. 191 (2020) 108662. https://doi.org/10.1016/j.matdes.2020.108662

13. I. Sabirov et al., Bulk Nanostructured Materials with Multifunctional Properties, Springer Briefs in Materials, https://doi.org/10.1007/978-3-319-19599-5_1

14. G.H. Lee, C.K. Rhee, M.K. Lee, W.W. Kim, V.V. Ivanov. Nanostructures and mechanical properties of copper compacts prepared by magnetic pulsed compaction method. Mater. Sci. Eng. A, 375–377 (2004) 604-608. https://doi.org/10.1016/j.msea.2003.10.100.

15. A. Bokov, G. Boltachev, N. Volkov, S. Zayats, A. Il'ina, A. Nozdrin, et al., Uniaxial compaction of nanopowders on a magnetic-pulse press. Tech. Phys. 58 (2013) 58. 1459–1468. https://doi.org/10.1134/S106378421310006X.

16. A. Pervikov, E. Glazkova, M. Lerner, Energy characteristics of the electrical explosion of two intertwined wires made of dissimilar metals. Phys. Plasmas 25 (2018) 070701. https://doi.org/10.1063/1.5034184.

17. V.M. Romanova, A.R. Mingaleev, A.E. Ter-Oganesyan, T.A. Shelkovenko, G.V. Ivanenkov, S.A. Pikuz, Core structure and secondary breakdown of an exploding wire in the current-pause regime, Matter Radiat. Extremes. 4 (2019) 026401. https://doi.org/10.1063/1.5085487.

18. V.M. Romanova, G.V. Ivanenkov, E.V. Parkevich, I.N. Tilikin, M.A. Medvedev, T.A. Shelkovenko, et al., Laser scattering by submicron droplets formed during the electrical explosion of thin metal wires. J. Phys. D: Appl. Phys. 54 (2021) 175201. https://doi.org/10.1088/1361-6463/abdce5.

19. G.S. Sarkisov, P.V. Sasorov, K.W. Struve, D.H. McDaniel, State of the metal core in nanosecond exploding wires and related phenomena. J. Appl. Phys. 96 (2004) 1674. https://doi.org/10.1063/1.1767976.

20. S.I. Tkachenko, A.R. Mingaleev, V.M. Romanova, A.E. Ter-Oganes'yan, T.A. Shelkovenko, S.A. Pikuz, Distribution of matter in the current-carrying plasma and dense core of the discharge channel formed upon electrical wire explosion, Plasma Phys. Rep., 35 (2009) 734. https://doi.org/10.1134/S1063780X09090037.

21. Yu. A. Kotov. The electrical explosion of wire: A method for the synthesis of weakly aggregated nanopowders. Nanotechnol. Russ., 4 (2009) 415–424. https://doi.org/10.1134/S1995078009070039

22. D. Dong, S. Fu, H. Jiang, G. Li, J. Cui, Study on the compaction characteristics of CNTs/TC4 composites based on electromagnetic warm compaction, J. Alloys Compd. 857 (2021) 158046. https://doi.org/10.1016/j.jallcom.2020.158046.

23. D. Dong, X. Huang, J. Cui, G. Li, H. Jiang, Effect of aspect ratio on the compaction characteristics and micromorphology of copper powders by magnetic pulse compaction, Adv. Powder Technol., 31 (2020) 4354-4364. https://doi.org/10.1016/j.apt.2020.09.010.

24. D. Dong, X. Huang, G. Li, J. Cui. Study on mechanical characteristics, microstructure and equation of copper powder compaction based on electromagnetic compaction, Mater. Chem. Phys. 253 (2020) 123449. https://doi.org/10.1016/j.matchemphys.2020.123449.

25. A. Pervikov, A. Khrustalyov, A. Filippov, Y. Mironov, A. Lozhkomoev, M. Lerner, et al., Structural, Mechanical, and Tribological Characterization of Magnetic Pulse Compacted Fe–Cu Bimetallic Particles Produced by Electric Explosion of Dissimilar Metal Wires. Metals 9 (12) (2019) 1287. https://doi.org/10.3390/met9121287.

26. S. Yan, S. Huang, W. Liu, J. Hu, Yu Lei, M. Zhou, Experimental and numerical investigation of temperature evolution during electromagnetic pulsed compaction of powders, Powder Technol., 306 (2017) 1-9. https://doi.org/10.1016/j.powtec.2016.11.014.

27. K. Peng, H. Pan, Z. Zheng, J. Yu, Compaction behavior and densification mechanisms of Cu – W composite powders. Powder Technol., 382 (2021) 478-490. https://doi.org/10.1016/j.powtec.2021.01.013.

28. A.S. Lozhkomoev, A.V. Pervikov, S.O. Kazantsev, A.F. Sharipova, N.G. Rodkevich, N.E. Toropkov, et al., Synthesis of Fe/Fe3O4 core-shell nanoparticles by electrical explosion of the iron wire in an oxygen-containing atmosphere. J. Nanopart. Res. 23 (2021) 73. https://doi.org/10.1007/s11051-021-05180-x.

29. A.V. Pervikov, K.V. Suliz, M.I. Lerner, Nanoalloying of clusters of immiscible metals and the formation of bimetallic nanoparticles in the conditions of non-synchronous explosion of two wires. Powder Technol. 360 (2020) 855-862. https://doi.org/10.1016/j.powtec.2019.11.003.

30. A.V. Pervikov, S.O. Kazantsev, A.S. Lozhkomoev, M.I. Lerner, Bimetallic Al-Ag, Al-Cu and Al-Zn nanoparticles with controllable phase compositions prepared by the electrical explosion of two wires, Powder Technol. 372 (2020) 136-147. https://doi.org/10.1016/j.powtec.2020.05.088.

31. J. Zhang, Y. Huang, Y. Liu, Z. Wang, Direct diffusion bonding of immiscible tungsten and copper at temperature close to Copper's melting point. Mater. Design 137 (2018) 473–480. https://doi.org/10.1016/j.matdes.2017.10.052

32. A. Debski, R. Debski, W. Gasior. New features of Entall database: comparison of experimental and model formation enthalpies. Arch. Metall. Mater. 59 (2014) 1337-1343. https://doi.org/10.2478/amm-2014-0228.

33. H. Mori, H.Y. Yasuda, Spontaneous alloying in nanometer-sized ultra-fine particles. Mater. Sci. Forum. 269-272 (1998) 327-332. https://doi.org/10.4028/www.scientific.net/MSF.269-272.327.

35. D. Choi. Phase transformation in thin tungsten films during sputter deposition. Microelectron. Eng. 183-184 (2017) 19-22. https://doi.org/10.1016/j.mee.2017.10.006

36. J.S. Lee, J. Cho, C.Y. You , Growth and characterization of α and β−phase tungsten films on various substrates, J. Vac. Sci. Technol. A. 34 (2016) 021502. https://doi.org/10.1116/1.4936261

37. H.L. Sun, Z.X. Song, D.G. Guo, F. Ma, K.W. Xu, Microstructure and mechanical properties of nanocrystalline tungsten thin films, J. Mater. Sci. Technol., 26(1) (2010) 87-92. https://doi.org/10.1016/S1005-0302(10)60014-X

38. L. Yanwei, Y. Xiaodong, T. Chengwen, S. Tiefeng, M. Kunsong, C. Hongnian, Effect of the β Phase on Compressive Mechanical Property of CVD Tungsten, Rare Metal Mat. Eng., 40(7) (2011) 1138-1140. https://doi.org/10.1016/S1875-5372(11)60045-3

39. Q. Hao, W. Chen, G. Xiao, Beta (b) tungsten thin films: Structure, electron transport, and giant spin Hall effect, Appl. Phys. Lett. 106 (2015) 182403. https://doi.org/10.1063/1.4919867.

40. D. Choi, K. Barmak, On the potential of tungsten as next-generation semiconductor interconnects, Electr. Mater. Lett. 13 (2017) 449–456. https://doi.org/10.1007/s13391-017-1610-5.

41. Y. Shen, Y. Mai, Influences of oxygen on the formation and stability of A15 β-W thin films. Mater Sci. Eng. A 284 (2000) 176–183. https://doi.org/10.1016/S0921-5093(00)00745-0.

42. W. Morcom, W. Worrell, H. Sell, H. Kaplan, The preparation and characterization of beta-tungsten, a metastable tungsten phase, Metall. Trans. 5 (1974) 155–161. https://doi.org/10.1007/BF02642939.

43. T. K. Sindhu, R. Sarathi, S. R. Chakravarthy, Understanding nanoparticle formation by a wire explosion process through experimental and modelling studies. Nanotechnology 19 (2007) 025703. https://doi.org/10.1088/0957-4484/19/02/025703.

44. R. Sarathi, T.K. Sindhu, S.R. Chakravarthy, Archana Sharma, K.V. Nagesh. Generation and characterization of nano-tungsten particles formed by wire explosion process. J. Alloys Compd. 475 (2009) 658-663. https://doi.org/10.1016/j.jallcom.2008.07.092.

45. H. Shi, X. Zou, X. Wang, Fully vaporized electrical explosion of bare tungsten wire in vacuum, Appl. Phys. Lett. 109 (2016) 134105. https://doi.org/10.1063/1.4963758.

46. F. Cardarelli Materials handbook. – London : Springer, 2018. – P. 2254.

47. B.I. Kostetsky, The structural-energetic concept in the theory of friction and wear (synergism and self-organization), Wear. 159 (1992) 1–15, https://doi.org/10.1016/0043-1648(92)90280-L.

48. A.A. Voevodin, C. Muratore, S.M. Aouadi, Hard coatings with high temperature adaptive lubrication and contact thermal management, Review, Surf. Coatings. Technol. 257 (2014) 247–265, https://doi.org/10.1016/j.surfcoat.2014.04.046.

49. A. Magn´eli, Structures of the ReO3-type with recurrent dislocations of atoms: `homologous series' of molybdenum and tungsten oxides. Acta Crystallogr. 6 (1953) 495–500.

50. C.C. Mardare, A.W. Hassel, Review on the versatility of tungsten oxide coatings. Phys Stat Sol A. 216 (2019) 1900047. https://doi.org/10.1002/pssa.201900047.

51. E. Lugscheider, O. Knotek, K. Bobzin, S Barwulf, Tribological properties, phase generation and high temperature phase stability of tungsten- and vanadium-oxides deposited by reactive MSIP-PVD process for innovative lubrication applications. Surf Coat Technol. 133 (2000) 134–362.

52. S.F. Gnyusov, E.A. Fedin, S. Yu. Tarasov, The effect of counterbody on tribological adaptation of an electron beam deposited HSS M2 steel coating in a range of sliding speeds and normal loads. Tribol. Int. 161 (2021) 107109. https://doi.org/10.1016/j.triboint.2021.107109.

53. W. Chena, P. Fenga, L. Dong, M. Ahangarkani, S. Ren, Y. Fu. The process of surface carburization and high temperature wear behavior of infiltrated W-Cu composites. Surf Coat Technol. 353 (2018) 300–308 https://doi.org/10.1016/j.surfcoat.2018.08.088